

Direction Finding Analysis of the 2012 July 6 Type II Solar Radio Burst at Low Frequencies

PERTTI MÄKELÄ,^{1,2} NAT GOPALSWAMY,² AND SACHIKO AKIYAMA^{1,2}

¹*The Catholic University of America
620 Michigan Ave., NE
Washington, DC 20064, USA*

²*NASA Goddard Space Flight Center
8800 Greenbelt Road
Greenbelt, MD 20771, USA*

(Accepted September 17, 2018)

Submitted to ApJ

ABSTRACT

The 2012 July 6 X1.1 flare at S13W59 and a halo coronal mass ejection (CME) with a space speed of $\sim 1900 \text{ km s}^{-1}$ were associated with type III and type II radio bursts. The metric-to-decametric type II radio burst extended down to $\sim 5 \text{ MHz}$. Simultaneously a slowly drifting feature with a harmonic structure was observed by Wind and STEREO radio receivers around and below 1 MHz, above the strong type III radio burst at lower frequencies. The radio direction finding analysis of this lower-frequency interplanetary (IP) type II radio burst indicates that the radio source was located near the nose and possibly towards the southern flank of the CME-driven shock. These results provide an independent confirmation of the previous suggestions that when the metric and IP type II bursts are overlapping, the lower-frequency IP type II radio burst originates near the shock nose, whereas the source of the higher-frequency metric type II burst is closer to the Sun in the shock flank region. These results further support the idea that the coronal and IP type II bursts are produced by the same CME-driven shock.

Keywords: Sun: coronal mass ejections (CMEs) — Sun: radio radiation — shock waves

1. INTRODUCTION

The first observations of type II solar radio bursts ranging from metric to kilometric wavelengths were made decades ago (Payne-Scott et al. 1947; Malitson et al. 1973). In dynamic radio spectra, type II bursts can be distinguished as continuous or intermittent bursts of radio emission slowly drifting downward in frequency (Wild & McCready 1950). Type II emission is caused by beams of electrons accelerated by a shock, which then generate Langmuir waves that are converted into radio waves at the fundamental or the first harmonic frequency, or both, of the local plasma near the shock (e.g. Melrose 1980; Nelson & Melrose 1985; Knock et al. 2001). Because the emission frequency depends on the electron density of the local plasma, it decreases as the shock propagates from the high-density low corona into the low-density interplanetary (IP) space. Fast coronal mass ejections (CMEs) are known to drive shocks that cause the lower-frequency decameter-hectometric (DH; Gopalswamy et al. 2001) and the kilometric type II bursts (Cane et al. 1987). The nature of the shocks producing metric type II burst has been more controversial. Both coronal blast waves and CME-driven shocks have been proposed as a source of metric type II bursts, and studies of metric type II observations have provided support for both suggestions (e.g. see discussion in Claßen & Aurass 2002; Cane & Erickson 2005; Gopalswamy 2006; Vršnak & Cliver 2008).

Another outstanding question of type II radio bursts considers the location of the radio source relative to the shock front. Mancuso & Raymond (2004) studied 29 metric type II bursts together with coronagraphic and spectrographic

observations of associated CMEs. They found that all type II bursts could be explained by a model where the type II radio emission originates in source locations above the nose or the flanks of the CME-driven shock. [Cho et al. \(2008\)](#) compared a selected set of 19 type II bursts with simultaneous CME observations by the Mauna Loa Solar Observatory (MLSO) MK coronagraphs and found that about half of the type II bursts were likely caused by a CME-streamer interaction and in the rest of the events the height of the CME leading edge and the formation height of the type II burst matched. In addition, the formation height of the type II bursts from CME-streamer interaction were below the CME leading edge but similar to the estimated CME-streamer interaction height suggesting that the radio source was at the flank of the shock. More recently [Ramesh et al. \(2012\)](#) found that most of the 41 limb CMEs associated with a metric type II burst had a radio source at or above the CME leading edge as observed by the Gauribidanur radioheliograph at 109 MHz. Several single event studies have found the shock-streamer interaction to be the source of metric type II bursts ([Shen et al. 2013](#); [Feng et al. 2015](#); [Zimovets & Sadykov 2015](#); [Lv et al. 2017](#)). Recently, [Al-Hamadani et al. \(2017\)](#) studied a selected set of 16 IP type II bursts and found that 6 (38%) of them were due to shock-streamer interaction.

A more specific set of type II radio bursts is composed by multi-lane bursts where type II emission lanes occur at separate frequencies, might be partially overlapping in time and have different drift rates, but do not resemble the well-known fundamental-harmonic or band-splitting structures ([Robinson & Sheridan 1982](#); [Gergely et al. 1984](#)). These multi-lane type II bursts have been studied mostly at metric wavelengths where they are more common. It has been suggested that they originate either from separate shocks or from different regions of a single shock ([Maxwell & Dryer 1982](#); [Reiner et al. 2001](#); [Leblanc et al. 2001](#); [Cho et al. 2011](#)). [Raymond et al. \(2000\)](#) reported on a multi-lane type II burst on 1998 June 11, where the higher-frequency type II emission occurred at metric wavelengths and the lower-frequency emission at decametric wavelengths. They suggest that the metric type II emission is caused by the CME-driven shock propagating in the higher density region within the streamer overlaying the source active region and the decametric type II emission originates from another section of the same shock propagating outside the streamer in a lower density region. These multi type II burst with simultaneous metric and DH emission are not as common as the complex type II bursts at metric wavelengths. [Gopalswamy \(2011\)](#) analyzed one such event that occurred on 2003 June 17. The two components of type II emission during this event were observed to start almost simultaneously. The starting frequency of the m-to-DH component was around 180 MHz and that of the DH-to-km component around 6 MHz. Their analysis supports the scenario where the shock flanks in the low corona are the source of the m-to-DH component and the shock nose higher in the corona is the source of the DH-to-km component.

The radio direction-finding (DF) techniques can be used to estimate the source location of solar radio bursts at long wavelengths from the measurements of radio receivers onboard spacecraft. Several different DF techniques have been suggested over the years (e.g. [Fainberg & Stone 1974](#); [Lecacheux 1978](#); [Manning & Fainberg 1980](#); [Santolík et al. 2003](#); [Ceconi & Zarka 2005](#); [Krupar et al. 2012](#); [Martínez Oliveros et al. 2012a](#)). The DF analysis relies on the anisotropic beaming pattern of the receiving antenna. The details of the DF techniques vary depending on whether the observing spacecraft is a spin-stabilized or a three-axis stabilized (non-spinning) spacecraft. Because reliable DF analysis requires sufficiently intense radio emission above the galactic background emission, the fast-drifting type III radio bursts that are more intense than type II radio bursts, were the first solar radio bursts at low-frequencies to be studied using the DF methods (e.g. [Fainberg et al. 1972](#); [Gurnett et al. 1978](#); [Reiner & Stone 1988](#)). Correspondingly, the more recent DF studies of type II radio bursts have concentrated on events with periods of more intense type II emission (e.g. [Hoang et al. 1998](#); [Reiner et al. 1998](#); [Martínez Oliveros et al. 2012b](#); [Magdalenic et al. 2014](#); [Martínez Oliveros et al. 2015](#); [Krupar et al. 2016](#); [Mäkelä et al. 2016](#)). The results of these single-event studies have confirmed that interaction of the CME-driven shocks with the pre-existing high-density structures such as streamers ([Reiner et al. 1998](#); [Magdalenic et al. 2014](#); [Martínez Oliveros et al. 2015](#); [Krupar et al. 2016](#)) or preceding CMEs ([Martínez Oliveros et al. 2012b](#); [Mäkelä et al. 2016](#)) result in favorable source regions for intense type II emission.

In this work, we investigate the location of the radio source of an IP type II radio burst on 2012 July 6 relative to the CME-driven shock. This event belongs to the special set of multi-lane type II radio bursts, where the metric and IP type II bursts are observed to overlap in time. The radio source location of the lower-frequency IP type II lane is estimated using DF method and the results are compared with white-light images of the associated CME. We analyse radio measurements from the WAVES investigation ([Bougeret et al. 1995](#)) on the Wind spacecraft and from the SWAVES experiment ([Bougeret et al. 2008](#)) on the Solar Terrestrial Relations Observatory (STEREO) spacecraft. White-light images are provided by the Large Angle and Spectrometric Coronagraph (LASCO; [Brueckner et al. 1995](#))

on the Heliospheric and Solar Observatory (SOHO) spacecraft and from the Sun Earth Connection Coronal and Heliospheric Investigation (SECCHI; Howard et al. 2008) on STEREO spacecraft.

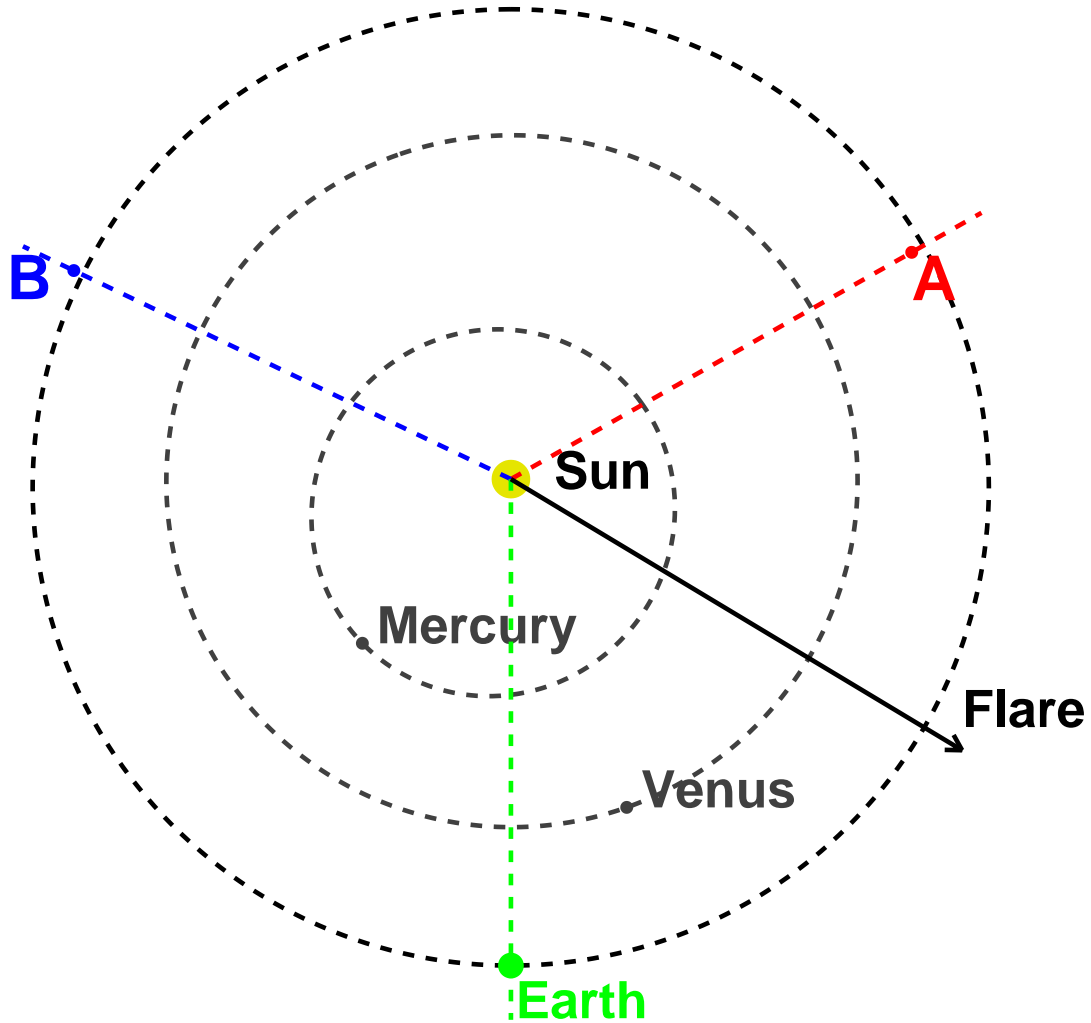


Figure 1. Locations of the STEREO spacecraft plotted at 23:24 UT on 2012 July 6 (the SOHO/LASCO CME observation time). The SOHO and Wind spacecraft are located near Earth around the Lagrange L1 point. In addition, the flare longitude of W59 (black arrow) is plotted together with the locations and orbits of Mercurius, Venus, and Earth.

2. OBSERVATIONS AND DATA

The 2012 July 6 type II radio burst was associated with a fast halo CME with a measured sky-plane speed of 1828 km s^{-1} and an estimated space speed of 1907 km s^{-1} according to the CDAW halo list (https://cdaw.gsfc.nasa.gov/CME_list/halo/halo.html). The halo CME was first observed at 23:10 UT by SECCHI/COR1-A coronagraph. The first detection by the LASCO/C2 coronagraph occurred at 23:24 UT. Gopalswamy et al. (2014) fitted a graduated cylindrical shell (GCS) model (Thernisien 2011) to the white-light images of SOHO and STEREO and found the peak velocity of the CME flux rope to be 2464 km s^{-1} . The GCS fitting also indicated a possible deflection of the CME to the south. The halo CME was associated with an X1.1 soft X-ray flare at S13W59 in NOAA active region 11515. The flare onset was at 23:01 UT and it reached the peak intensity at

23:08 UT. A preceding CME with a sky-plane speed of 660 km s^{-1} from the same AR 11515 as the primary CME was observed at 10:36 UT by LASCO/C2. This CME had a narrow width of 67° and it was associated with an M1.8 soft X-ray flare at S17W42. The progress of the halo CME from the low corona into IP space could be followed by the SOHO/LASCO C2 and C3 coronagraphs (Brueckner et al. 1995) and STEREO/SECCHI COR1 and COR2 coronagraphs and the HI1 heliospheric imager (Howard et al. 2008). The relative locations of the SOHO (near Earth) and STEREO spacecraft are shown in Fig. 1. The heliographic longitudes of STEREO-A and STEREO-B spacecraft were W120 and E115, respectively. The arrow in Fig. 1 indicates the flare longitude of W59. Hence, the longitudinal separation between the solar source (assumed to be the flare site) and the SOHO and STEREO-A spacecraft were almost the same, 59° and 61° , respectively. From the viewpoint of STEREO-B spacecraft, the eruption was nearly perfectly back-sided event with the source separation angle of 174° .

Gopalswamy et al. (2016) reported that the initial CME acceleration was 5.87 km s^{-2} , the second largest among SEP-producing CMEs in cycles 23 and 24 (see their Table 2). The CME initial speed was estimated to be $> 3000 \text{ km s}^{-1}$. Long et al. (2017) found that the EIT wave associated with the halo CME eruption had an unusually high mean speed of 1106 km s^{-1} as observed by the Atmospheric Imaging Assembly (AIA; Lemen et al. 2012) on the Solar Dynamics Observatory (SDO) and Extreme UltraViolet Imager (EUVI) of the SECCHI instrument suite on STEREO-A spacecraft. The high speed of the EIT wave indicate that initial acceleration of the CME must have been high as suggested by Gopalswamy et al. (2016). The fast CME acceleration is also consistent with the report by the Palehua Solar Observatory of the Radio Solar Telescope Network (RSTN) that reported the onset of the metric type II burst at 23:09 UT, only about one minute after the peak time of the flare. The relative timing of the peak of the X-ray flare and the onset of the metric type II confirms the finding by Zhang et al. (2001) that the impulsive acceleration phase of CMEs coincides with the rise phase of the associated flares. The metric type II radio burst was observed also by the Culgoora and Hiraiso radio spectrographs. The measurements of the 2012 July 6 type II radio burst at the DH and kilometric wavelengths are provided by the Wind/WAVES (Bougeret et al. 1995) and STEREO/WAVES (SWAVES) (Bougeret et al. 2008) radio experiments. The top panel of Fig. 2 shows the combined plot of the Culgoora and WAVES dynamic spectra, and the dynamic spectrum from the SWAVES experiment on the STEREO-A spacecraft is plotted in the top panel of Fig. 3. The WAVES spectrum shows that the metric type II continued down at least to the frequency of 8 MHz. The metric type II ends around 23:55 UT. The Wind data are from the RAD2 (1.075–13.825 MHz) and RAD1 (20–1040 kHz) receivers of the WAVES experiment. In the SWAVES dynamic spectrum, the measurements in the 125 kHz – 16.025 MHz range are from the High Frequency Receiver (HFR) and in the 2.5–160 kHz range from the Low Frequency Receiver (LFR).

The specialty of this event is that a second type II radio burst with a fundamental-harmonic structure is seen to start at lower frequencies before the end of the metric type II burst. The top panel of Fig. 2, a narrow harmonic lane is seen first around 23:25 UT just above 1 MHz. The fundamental lane is seen superposed in the beginning with the dominant type III radio burst until about 23:40 UT. The fundamental emission component is more intense and the frequency range is wider than those of the harmonic emission component that fades away around 00:15 UT on 2012 July 7. We like to emphasize that we have plotted the data of different receivers in arbitrary units and especially we have adjusted the scaling of the data so that the fainter features, especially the narrow-band harmonic lane of the lower frequency type II is clearly visible. The fundamental drifts slowly down to 350 kHz before it disappears around 00:52 UT on 2012 July 7. The top panel of Fig. 3 shows similar overall behavior observed by SWAVES-A. However, the intensity and the duration of the type II emission are reduced. The harmonic emission component is almost invisible, and the fundamental emission component is seen to drift down to 400 kHz before fading away around 00:50 UT. The weaker intensity of type II emission measured by SWAVES-A could indicate that the type II emission was more directed towards Wind spacecraft. In addition, the lower sensitivity due to shorter antennas affects the STEREO radio observations. Measurements of both WAVES and SWAVES-A have short-duration data gaps.

For the DF analysis of the WAVES measurements, we use data only from the RAD1 receiver. Because the Wind is a spinning spacecraft, the source location of the radio source relative to the Wind spacecraft is calculated from the modulation of the antenna signal due to the spacecraft spin (Fainberg et al. 1972). In the case of the SWAVES experiment, we analyze the HFR data. Contrary to the Wind spacecraft, the STEREO spacecraft are three-axis stabilized, therefore, the arrival direction of the radio waves is estimated using the onboard-calculated autocorrelations and cross-correlations of the antenna signals (see Martínez Oliveros et al. 2012a).

3. RESULTS

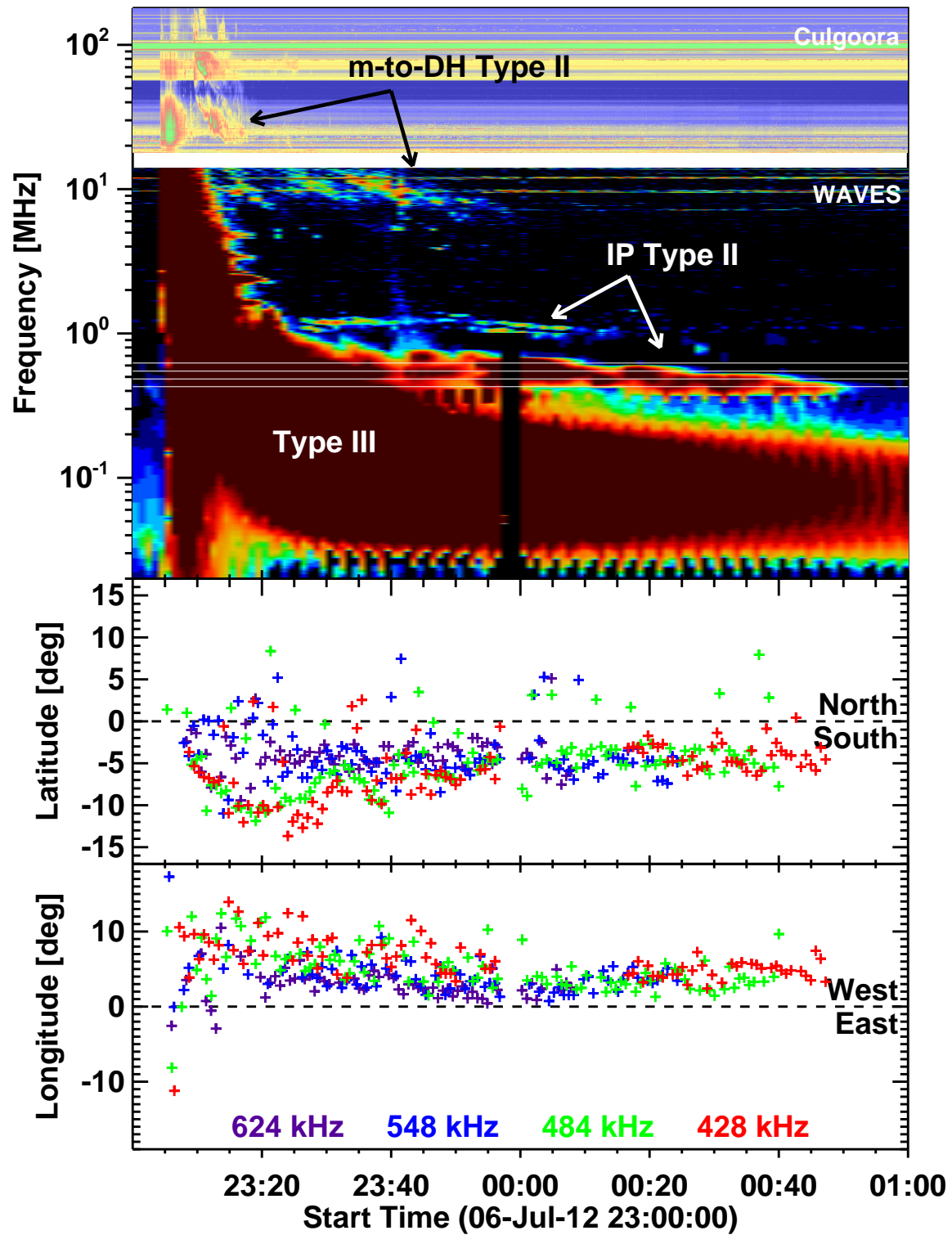


Figure 2. Results of the DF analysis of the Wind/WAVES measurements at four frequencies between 428 kHz and 624 kHz. The top-most panel shows the combined Culgoora and Wind/WAVES radio dynamic spectra. The type III, the m-to-DH and IP type II radio bursts are indicated. The white horizontal lines mark the four frequencies used in the DF analysis. The two lower panels show the DF results for the radio source location: the latitude relative to the ecliptic plane and the longitude relative to the Sun-spacecraft direction.

The lower panels of Fig. 2 summarize the DF results for the WAVES instrument on the Wind spacecraft. We used four frequencies of 624 kHz, 548 kHz, 484 kHz, and 428 kHz for the DF analysis. The white horizontal lines on the top panel of Fig. 2 mark the measurement frequencies. The middle panel shows direction of the oncoming radio emission as the latitude relative to the ecliptic plane and the bottom panel as the longitude relative to the Sun-Wind line. In the beginning, emission from the type III radio burst dominates at all four frequencies, but around and after the end of the data gap at 00 UT July 7, the emissions observed at the four frequencies are mostly type II emission. Because the accuracy and reliability of the DF analysis depends on the signal-to-noise ratio, the highest frequency of 624 kHz is useful only for a brief period after the data gap until about 00:05 UT, whereas the signal at the lowest frequency becomes strong enough after about 00:15 UT on July 7, and lasts until the type II bursts fade away around 00:50 UT. The middle panel of Fig. 2 reveals that the latitude of the type II source direction does not have large differences between the four frequencies. Whereas, the longitude plot at the bottom panel of Fig. 2 shows that the type II source has the most western location relative to the Sun-Wind line at the lowest frequency of 428 kHz. The westernmost location is in agreement with the decrease in the electron density of the plasma as a function of the distance, which entails that the type II radio source at the lowest frequency should have the largest distance from the Sun.

A summary of the DF analysis results from the SWAVES-A measurements is shown in Fig. 3. The observed type II emission at the STEREO-A spacecraft in the frequency range of 500–700 kHz is weaker and also the burst durations is shorter than those observed at the Wind spacecraft. The low-frequency type II burst extends from about 23:45 UT on July 6 to about 00:50 on 2012 July 7. Again, we have analysed SWAVES-A data from four measurements frequencies of 675 kHz, 625 kHz, 575 kHz, and 525 kHz, marked with white horizontal lines on the top panel of Fig. 3. Again, the source latitude plotted in the middle panel of Fig. 3 does not indicate clear difference between the four frequency measurements, whereas from the bottom panel we can see that the type II source at the lowest frequency of 525 kHz has the most eastern locations as seen from the STEREO-A spacecraft.

We have compared the type II source directions obtained from the WAVES and SWAVES-A radio measurement with the white-light images of the associated CME. Figure 4 shows the estimated radio source locations from the WAVES DF analysis at the 624 kHz frequency plotted on the LASCO/C3 running difference image at 00:06 UT on 2012 July 7. The times of the radio observations and the corresponding location of the centroid of the type II source at that time are color coded and plotted on the image. The radio observation times precede the LASCO/C3 image time only by a few minutes. The location of the shock front relative to the brighter CME behind it is uncertain, but especially the source location at 00:03:17 UT appears to be exactly on the nose region of the shock. The source locations at the earlier times are located slightly towards the southern side of the shock nose and are also at larger radial distances. Considering the fluctuations in the estimated latitude and longitude of the radio source shown in Fig. 2 and the fact that one degree change in the direction angle at 1 AU corresponds about $3.8 R_{\odot}$ distance on the sky-plane, the scatter of source locations relative to the CME is in the expected range.

A similar comparison of the SWAVES-A directions with the combined image of SECCHI/COR2-A and HI1-A images is shown in Fig. 5. The running difference images of HI1-A was taken at 00:09:01 UT and COR2-A at 00:24 UT. Again, the time of the radio measurement precedes the image times by minutes to tens of minutes. The halo CME is still in the COR2 field of view. The location of the shock front in the COR2 image is uncertain, because the leading edge of the CME is not smooth. The nose of the CME is located where a loop-like structure appears in the COR2 image around the position angle 125° . The type II source locations (colored circles) are at larger radial distances than the nose of the CME, but clearly the majority of them are above the nose direction of the CME. Therefore, both Figs. 4 and 5 indicate that the most likely location of the low-frequency type II radio burst is near the nose of the shock. However, it is clear that the DF source locations do not fall on the leading edge of the CME, instead, they appear at larger radial distances. The shift in location is probably caused by scattering of the radio waves in the IP medium. For example, Mäkelä et al. (2016) noticed in their study of the 2013 May 22 CME-CME interaction event that radio source directions at the frequencies below ~ 800 kHz appeared to be shifted away from the Sun.

The accuracy of the derived direction of the radio source has been estimated previously. Based on their experience in analyzing solar and planetary radio emissions Reiner et al. (2009) state that the location of the radio source using Wind observations can be determined to the accuracy of one degree or less. Cecconi & Zarka (2005) estimated for their DF technique that the accuracy of the source location measured by receivers on three-axis stabilized spacecraft, such as the SWAVES receiver, to be of the order of 1° – 2° . However, the estimated source direction is always based on in-situ measurements and scattering effects during wave propagation may change the wave arrival direction as mentioned. Krupar et al. (2014) studied type III radio bursts, which are fast drifting radio bursts produced by beams

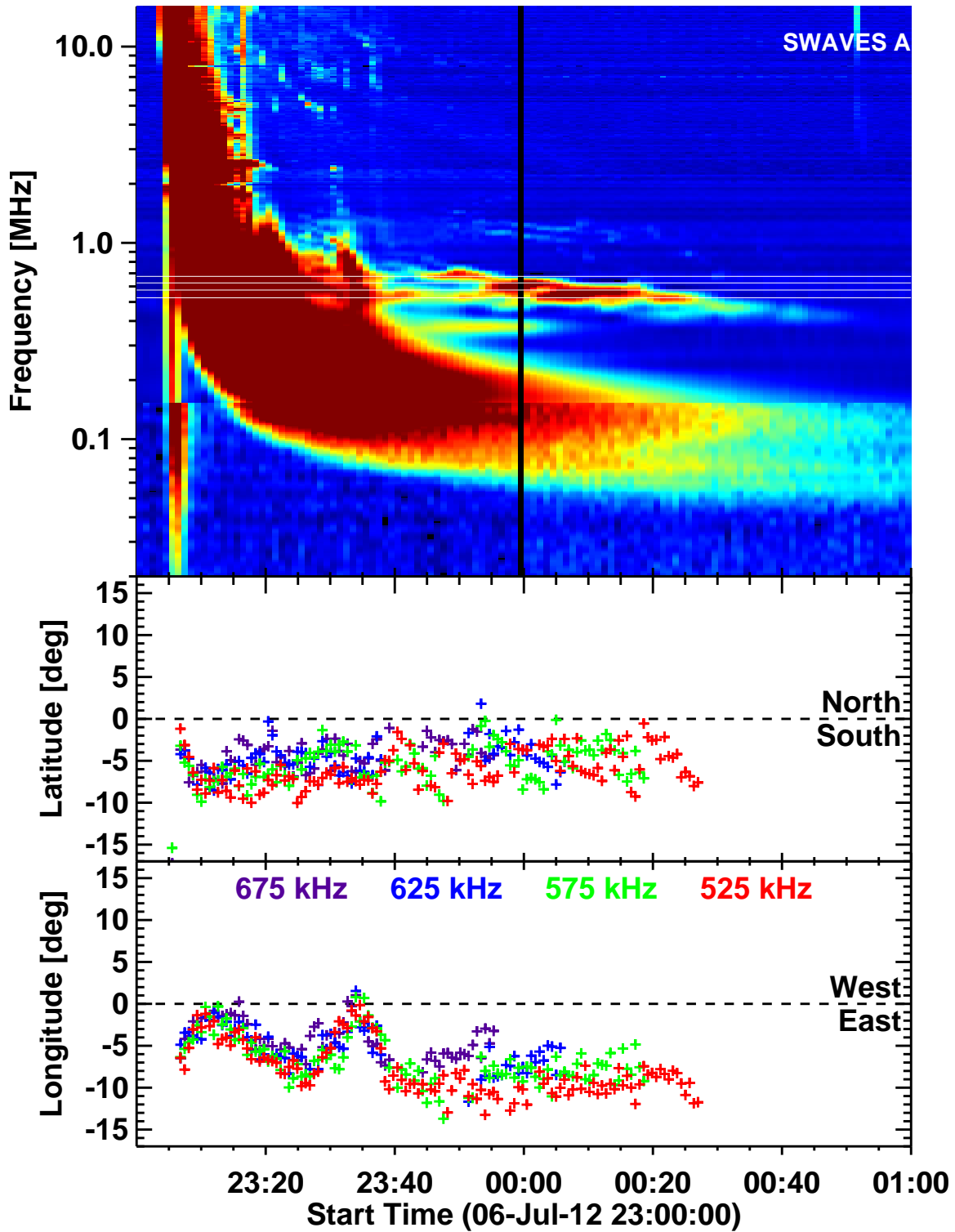


Figure 3. Results of the DF analysis of the SWAVES-A measurements at four frequencies between 525 kHz and 675 kHz. The top-most panel shows the SWAVES-A radio dynamic spectra. The white horizontal lines mark the four frequencies used in the DF analysis. The two lower panels show the DF results for the radio source location: the latitude relative to the ecliptic plane and the longitude relative to the Sun-spacecraft direction.

of flare-accelerated electrons propagating along the Parker spiral of the IP magnetic field. In addition, the radio emission of type III bursts is more intense than that of type II bursts, which make them more suitable for DF analysis.

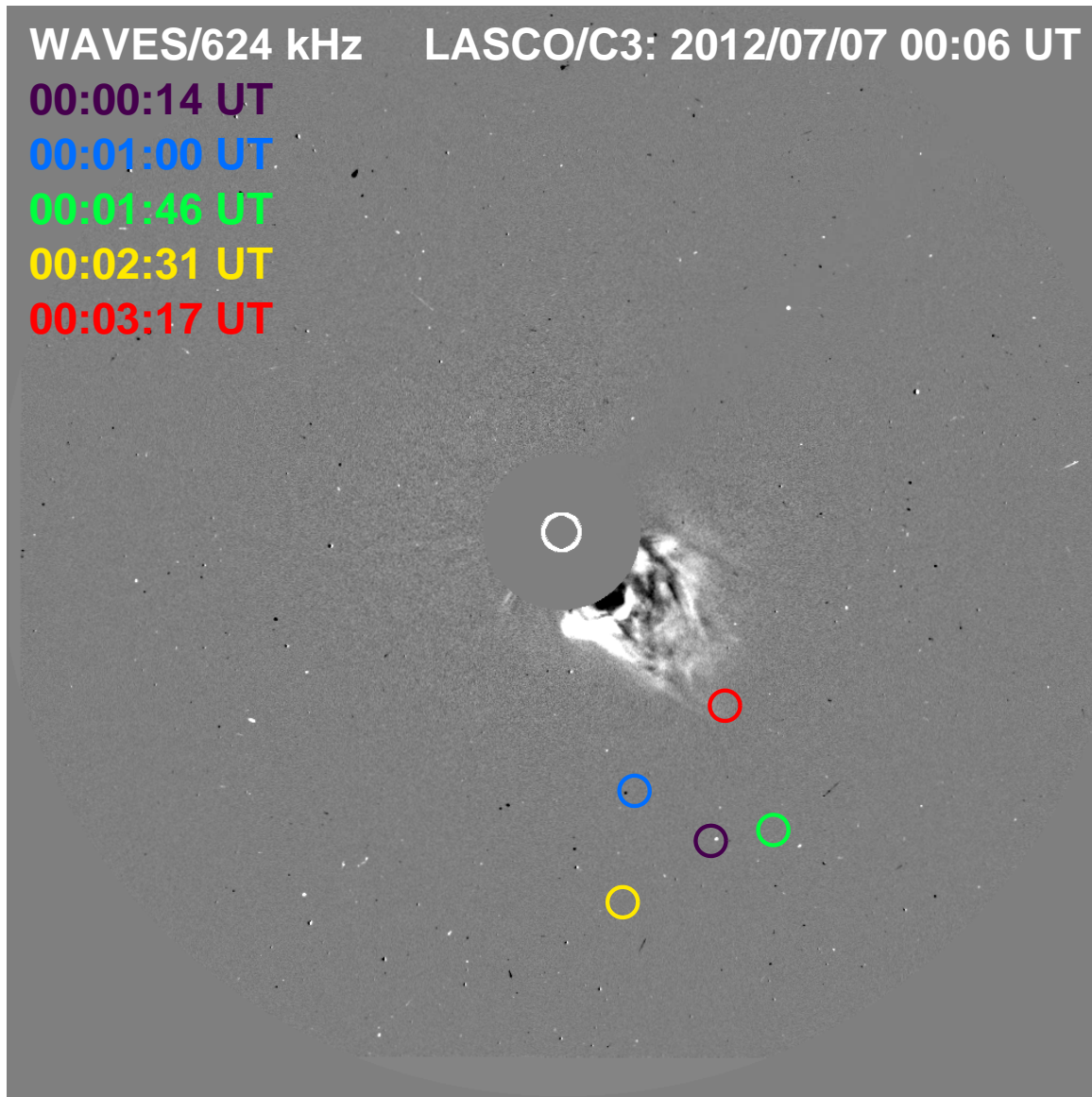


Figure 4. The radio source locations over-plotted on the LASCO/C3 running difference image at 00:06 UT on 2012 July 7 suggest that the nose region of the CME propagating towards south-west in the LASCO field of view was the source of the IP type II emission.

In their statistical study of a large set of type III bursts, [Krupar et al. \(2014\)](#) found a good agreement between the Parker spiral and the source locations of type III bursts estimated at frequencies above 700 kHz. But they also suggest that at lower frequencies the radio source locations are shifted due to scattering effects during radio wave propagation.

Another issue that might affect the source location estimates is the spatial extent of the radio source. The distribution of the emission intensity within the source region or how it might evolve over time are also poorly known. The different DF techniques usually assume a point-like radio source, when deriving the source direction. Because type II radio bursts are associated with CME-driven shock, which are large-scale structures, it is likely that the radio source is extended instead of being point-like. However, [Cecconi \(2007\)](#) investigated the location error of extended radio sources measured by a three-axis stabilized spacecraft and found that for radio sources with an angular half width smaller than 5° the source direction errors are about 1° or less. These results are similar to the results obtained in the earlier study by [Cecconi & Zarka \(2005\)](#), where they assumed a point-like structure. Because the apparent size of the radio source, which can be also derived from DF analysis, includes both spatial extent and wave propagation effects, the interpretation of the obtained result is difficult and beyond our analysis.

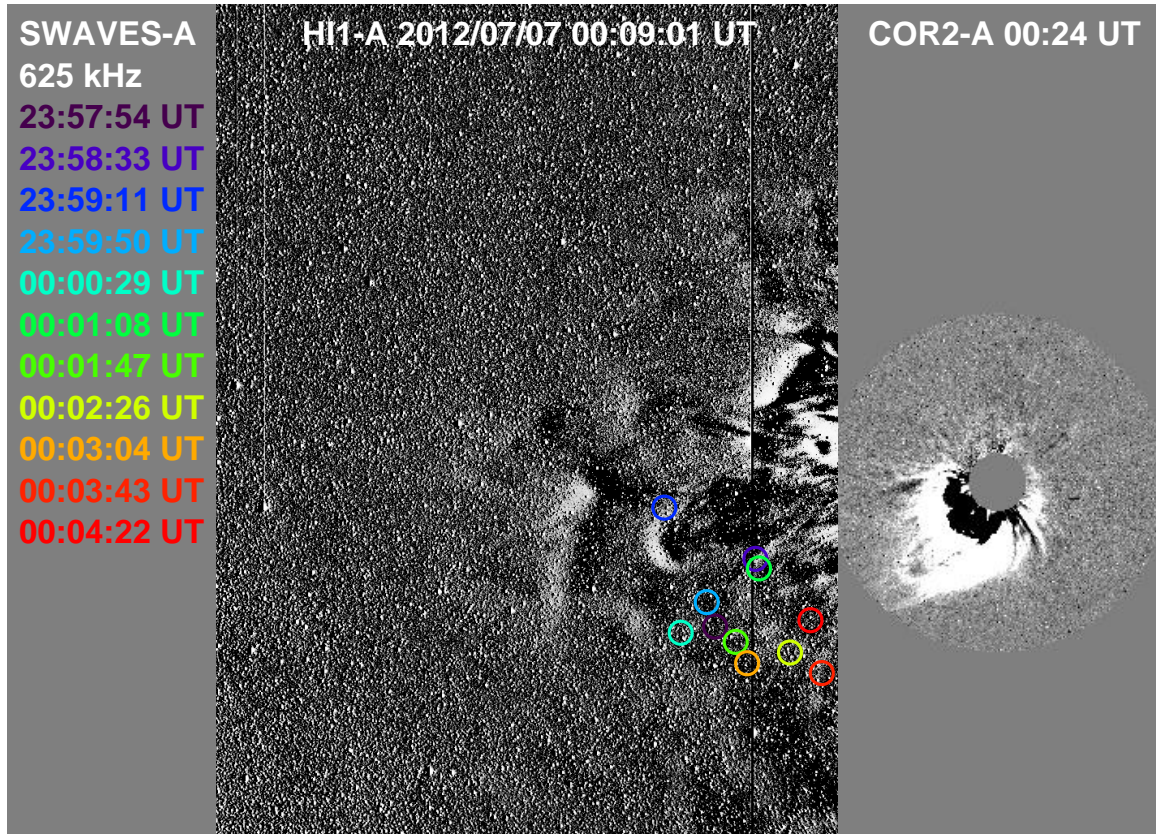


Figure 5. The radio source locations over-plotted on the combined HI1-A (00:09 UT) and COR2-A (00:24 UT) running difference images on 2012 July 7 suggest that the nose region of the CME propagating towards south-east in the STEREO field of view was the source of the IP type II emission.

Triangulation can be used to estimate the source location in 3D space if one can obtain the DF source directions from two or more spacecraft at separate locations. However, the analyzed frequencies must be close enough, otherwise the type II emission cannot originate from the same source location, because the electron number density levels corresponding to each frequency are too far apart. In our case, only the pair of SWAVES-A and WAVES frequencies at 625 kHz and 624 kHz are close enough for us to attempt triangulation. Unfortunately, the WAVES measurements had a data gap before 00:00 UT on 2012 July 7. However, for the short period after the 00:00 UT until about 00:06 UT on July 7 both SWAVES-A and WAVES observed a strong signal of type II emission at these frequencies. The average latitude and longitude of the radio source from SWAVES-A measurement during this time period were -5.2° and -6.6° , respectively. The minus sign indicates that the source directions was south of the ecliptic plane and towards east from the STEREO-A-Sun line. The average latitude and longitude obtained from WAVES measurement were -4.3° and 2.4° , respectively. Therefore, the source was seen from Wind spacecraft to be south of the ecliptic and towards west of the Wind-Sun line. The lines drawn from the spacecraft along the apparent source directions do not cross each, but the nearest points of the two lines can be calculated. The radial distance of the type II source calculated from the midpoint of the line connecting the two nearest points is about $26.9 R_\odot$. This is much larger distance than the measured CME height around that time. The sky-plane height of the CME leading edge measured from LASCO/C3 image at 00:06 UT was $11.81 R_\odot$. If we apply a simple projection effect correction to this apparent height by dividing it by $\sin(59^\circ)$, because the longitude of the solar source (flare) was at W59, we get an estimated CME height of $13.8 R_\odot$. Another simple method to correct the projection effects in the CME height measurements is to multiply the measured sky-plane height by the ratio of the space speed to the sky-plane speed. If we use the CME peak speed estimated by Gopalswamy et al. (2016) using the GCS model fitting, we obtain the corrected height of $15.9 R_\odot$ for the CME leading edge. Even if we take into account the stand-off distance of the shock front, the radial distance obtained from triangulation is larger than the CME height estimated from the white-light images. The discrepancy between the radial distance from radio measurements and the white-light measurements likely indicates that the DF source

locations at the analyzed frequencies are shifted away from the Sun due to radio wave scattering (see e.g. Mäkelä et al. 2016).

4. SUMMARY

We compared the DF radio source directions of an IP type II radio burst with the white-light images of the associated CME observed 2012 July 6–7 by the SOHO and STEREO coronagraphs and heliospheric imagers. The estimated space speed of the CME was 1907 km s^{-1} and the CME was associated with an X1.1 soft X-ray flare at S13W59 according to the CDAW Halo CME list. The Wind/WAVES DF analysis of the IP type II burst showed the radio sources close to the nose region of the CME as seen in the LASCO/C3 images. Similarly the SWAVES-A DF analysis indicated radio sources near the nose region of the CME as seen in the SECCHI COR2-A and HI1-A images. However, the radio source locations were shifted away from the Sun and the leading edge of the associated CME, probably due to scattering of the radio waves. The results confirm earlier suggestions that when metric and IP type II radio bursts overlap in time, the radio source of the lower-frequency IP type II burst must be near the shock nose region.

We thank the Wind, SOHO and STEREO teams for providing data. SOHO is a project of international cooperation between ESA and NASA. The SWAVES-A data is provided by the CDDP data archive at <http://cdpp-archive.cnes.fr>. PM was in part supported by the NSF grant AGS-1358274. The work of NG was supported by NASA/LWS program. SA was in part supported by the NSF grants AGS-1622377 and AGS-1358274.

REFERENCES

- Al-Hamadani, F., Pohjolainen, S., Valtonen, E. 2017, *SoPh*, 292, 127
- Bougeret, J.-L., Kaiser, M. L., Kellogg, P. J., et al. 1995, *SSRv*, 71, 231
- Bougeret, J.-L., Goetz, K., Kaiser, M. L., et al. 2008, *SSRv*, 136, 487
- Bueckner, G. E., Howard, R. A., Koomen, M. J., et al. 1995, *SoPh*, 162, 357
- Cane, H. V., Sheeley, Jr, N. R., & Howard, R. A. 1987, *JGR*, 92, 9869
- Cane, H. V., & Erickson, W. C. 2005 *ApJ*, 623, 1180
- Cecconi, B. 2007, *RaSc*, 42, RS2003
- Cecconi, B., & Zarka, P. 2005, *RaSc*, 40, RS3003
- Cho, K.-S., Bong, S.-C., Kim, Y.-H., et al. 2008, *A&A*, 491, 873
- Cho, K.-S., Bong, S.-C., Moon, Y.-J., et al. 2011, *A&A*, 530, A16
- Claßen, H. T. & Aurass, H. 2002, *A&A*, 384, 1098
- Fainberg, J., Evans, L. G., & Stone, R. G. 1972, *Science*, 178, 743
- Fainberg, J., & Stone, R.-G. 1974, *SSRv*, 16, 145
- Feng, S. W., Du, G. H., Chen, Y., Kong, X.L., Li, G., & Gou, F. 2015, *SoPh*, 290, 1195
- Gergely, T. E., Kundu, M. R., Wu, S. T., et al. 1984, *AdSpR*, 4, 283
- Gopalswamy, N. 2006, *GMS*, 165, 207
- Gopalswamy, N. 2011, *Planetary Radio Emissions VII*, ed. H. O. Rucker, W. S. Kurth, P. Louarn, & G. Fischer (Vienna: Austrian Academy of Sciences Press), 325
- Gopalswamy, N., Yashiro, S., Kaiser, M. L., Howard, R. A., & Bougeret, J.-L. 2001, *JGR*, 106, 29219
- Gopalswamy, N., Xie, H., Akiyama, S., Mäkelä, P., & Yashiro, S. 2014, *EP&S*, 66, 104
- Gopalswamy, N., Yashiro, S., Thakur, N., et al. 2016, *ApJ*, 833, 216
- Gurnett, D. A., Baumbach, M. M., & Rosenbauer, H. 1978, *JGR*, 83, 616
- Hoang, S., Maksimovic, M., Bougeret, J.-L., Reiner, M. J., & Kaiser, M. L. 1998, *GeoRL*, 25, 2497
- Howard, R. A., Moses, J. D., Vourlidas, A., et al. 2008, *SSRv*, 136, 67
- Knock, S. A., Cairns, I. H., Robinson, P. A., & Kuncic, Z. 2001, *JGR*, 106, 25041
- Krupar, V., Santolik, O., Cecconi, B., et al. 2012, *JGR*, 117, A06101
- Krupar, V., Maksimovic, M., Santolik, O., Cecconi, B., & Kruparova, O. 2014, *SoPh*, 289, 4633
- Krupar, V., Eastwood, J. P., Kruparova, O., et al. 2016, *ApJL*, 823, L5
- Leblanc, Y., Dulk, G. A., Vourlidas, A., Bougeret, J.-L. 2001, *JGR*, 106, 25301
- Lemen, J. R., Title, A. M., Akin, D. J., et al. 2012, *SoPh*, 275, 17
- Lecacheux, A. 1978, *A&A*, 70, 701
- Long, D. M., Valori, G., Pérez-Suárez, D., Morton, R. J., & Vásquez, M. 2017, *A&A*, 603, A101
- Lv, M. S., Chen, Y., Li, C. Y., et al. 2017, *SoPh*, 292, 194

- Magdaleníć, J., Marqué, C., Krupar, V., et al. 2014, *ApJ*, 791, 115
- Malitson, H. H., Fainberg, J., & Stone, R. G. 1973, *ApJ*, 183, L35
- Mäkelä, P., Gopalswamy, N., Reiner, M. J. 2016, *ApJ*, 827, 141
- Mancuso, S., & Raymond, J. C. 2004, *A&A*, 202, 363
- Manning, R., & Fainberg, J. 1980, *SSI*, 5, 161
- Martínez Oliveros, J. C., Lindsey, C., Bale, S. D., & Krucker, S. 2012a, *SoPh*, 279, 153
- Martínez Oliveros, J. C., Raftery, C. L., Bain, H. M., et al. 2012b, *ApJ*, 748, 66
- Martínez Oliveros, J. C., Raftery, C., Bain, H., et al. 2015, *SoPh*, 290, 891
- Maxwell, A., & Dryer, M. 1982, *SSRv*, 32, 11
- Melrose, D. B. 1980, *SSRv*, 26, 3
- Nelson, G. J., & Melrose, D. B., 1985, in *Solar radiophysics: Studies of emission from the sun at metre wavelengths*, ed. D. J. McLean & N. R. Labrum (Cambridge and New York: Cambridge University Press), 333
- Payne-Scott, R., Yabsley, D. E., & Bolton, J. G. 1947, *Nature*, 160, 256
- Ramesh, R., Anna Lakshmi, M., Kathiravan, C., Gopalswamy, N., & Umapathy, S. 2012, *ApJ*, 752, 107
- Raymond, J. C., Thompson, B. J., St. Cyr, O. J., et al. 2000, *GeoRL*, 27, 1439
- Reiner, M. J., & Stone, R. G. 1988, *A&A*, 206, 316
- Reiner, M. J., Kaiser, M. L., Fainberg, J., & Stone, R. G. 1998, *JGR*, 103, 29651
- Reiner, M. J., Kaiser, M. L., Gopalswamy, N., et al. 2001, *JGR*, 106, 25279
- Reiner, M. J., Goetz, K., Fainberg, M. L., et al. 2009, *SoPh*, 259, 255
- Robinson, R. D., & Sheridan, K. V. 1982, *PASAU*, 4, 392
- Santolík, O., Parrot, M., & Lefeuvre, F. 2003, *RaSc*, 38, 1010
- Shen, C., Liao, C., Wang, Y., Ye, P. & Wang, S. 2013, *SoPh*, 282, 543
- Thernisien, A. 2011, *ApJS*, 194, 33
- Vršnak, B. & Cliver, E. W. 2008, *SoPh*, 253, 215
- Wild, J. P. & McCready, L. L. 1950, *AuSRA*, 3, 387
- Zhang, J., Dere, K. P., Howard, R. A., Kundu, M. R., & White, S. M. 2001, *ApJ*, 559, 452
- Zimovets, I. V. & Sadykov, V. M. 2015, *AdSpR*, 56, 2811